

**Spin density studies on  $p$ -O<sub>2</sub>NC<sub>6</sub>F<sub>4</sub>CNSSN: A heavy  $p$ -block organic ferromagnet**J. Luzon,<sup>1,2</sup> J. Campo,<sup>1,\*</sup> F. Palacio,<sup>1</sup> G. J. McIntyre,<sup>2</sup> J. M. Rawson,<sup>3</sup> R. J. Less,<sup>3</sup> C. M. Pask,<sup>3</sup> A. Alberola,<sup>3</sup> R. D. Farley,<sup>4</sup> D. M. Murphy,<sup>4</sup> and A. E. Goeta<sup>5</sup><sup>1</sup>*Instituto de Ciencia de Materiales de Aragón, CSIC-Universidad de Zaragoza, Zaragoza 50009, Spain*<sup>2</sup>*Institut Laue-Langevin, 6 rue Jules Horowitz, 38042 Grenoble, France*<sup>3</sup>*Department of Chemistry, The University of Cambridge, Lensfield Road, Cambridge CB2 1EW, United Kingdom*<sup>4</sup>*School of Chemistry, Cardiff University, Main Building, Park Place, Cardiff CF10 3AT, United Kingdom*<sup>5</sup>*Department of Chemistry, University of Durham, South Road, Durham DH1 3LE, United Kingdom*

(Received 13 December 2009; revised manuscript received 4 March 2010; published 29 April 2010)

A complete picture of the spin density distribution in the organic radical  $p$ -O<sub>2</sub>NC<sub>6</sub>F<sub>4</sub>CNSSN has been obtained by a combination of polarized neutron diffraction, electron paramagnetic resonance (EPR), and electron-nuclear double resonance (ENDOR) spectroscopies, and *ab initio* density-functional theory (DFT) calculations. Polarized neutron diffraction revealed that the spin distribution is predominantly localized on the N and S atoms (+0.25 $\mu_B$  and +0.28 $\mu_B$ , respectively) of the heterocyclic ring with a small negative spin density on the heterocyclic C atom (−0.06 $\mu_B$ ). These spin populations are in excellent agreement with both *ab initio* DFT calculations (spin populations on the C, N, and S sites of −0.07, 0.22 and 0.31, respectively) and cw-EPR studies which estimated the spin population on the N site as 0.24. The DFT calculated spin density revealed less than 1% spin delocalization onto the perfluoroaryl ring, several orders of magnitude lower than the density on the heterocyclic ring. cw-ENDOR studies at both  $X$ -band (9 GHz) and  $Q$ -band (34 GHz) frequencies probed the spin populations on the two chemically distinct F atoms. These spin populations on the F atoms *ortho* and *meta* to the dithiadiazolyl ring are of magnitude 10<sup>−3</sup> and 10<sup>−4</sup>, respectively.

DOI: [10.1103/PhysRevB.81.144429](https://doi.org/10.1103/PhysRevB.81.144429)

PACS number(s): 75.50.Xx, 75.25.−j, 76.30.Rn, 31.15.ae

**I. INTRODUCTION**

The magnetic properties of organic free radicals have received considerable attention in recent years since the discovery of ferromagnetism in the  $\beta$  phase of the organic radical  $p$ -NPNN below 0.6 K.<sup>1</sup> Since then a number of organic magnets have been reported, mostly with ordering temperatures below 1 K. We employed a strategy to implement the more radially diffuse orbitals associated with heavier  $p$ -block elements such as S and Se to enhance exchange and raise magnetic ordering temperatures.<sup>2</sup> This has subsequently led to a number of other heavy  $p$ -block organic radicals with high magnetic ordering temperatures.<sup>3–5</sup> Among these radicals the family of dithiadiazolyl radicals has attracted particular attention.

In contrast to the majority of dithiadiazolyl radicals which associate to form spin-paired dimers in the solid state, we have found that a number of perfluorophenyl derivatives of general formula  $p$ -XC<sub>6</sub>F<sub>4</sub>CNSSN retain their free-radical nature in the solid state.<sup>2</sup> In particular,  $p$ -NCC<sub>6</sub>F<sub>4</sub>CNSSN has been studied extensively since one of its two solid-state forms undergoes a phase transition to a canted antiferromagnetic state below 36 K,<sup>6</sup> the highest reported temperature for a metal-free compound. Moreover, contrary to most organic magnets whose ordering temperature decreases as an external pressure is applied, the ordering temperature in this compound rises up to 72 K under an hydrostatic pressure of 19 kbar.<sup>7</sup> Additional derivatives  $p$ -BrC<sub>6</sub>F<sub>4</sub>CNSSN,<sup>8</sup>  $p$ -IC<sub>6</sub>F<sub>4</sub>CNSSN,<sup>9</sup> and  $p$ -NCC<sub>6</sub>F<sub>4</sub>C<sub>6</sub>F<sub>4</sub>CNSSN (Ref. 10) have also been found to not dimerize, although there has been no evidence for bulk magnetic order in these derivatives.

In this paper, we implement polarized neutron diffraction, electron paramagnetic resonance (EPR), and electron-nuclear

double resonance (ENDOR) spectroscopies to experimentally probe the spin density distribution in  $p$ -O<sub>2</sub>NC<sub>6</sub>F<sub>4</sub>CNSSN, which some of us have previously reported to exhibit ferromagnetism below 1.3 K.<sup>11</sup> In addition these experimental studies are supported by *ab initio* density-functional theory (DFT) calculations (Preliminary reports of selected aspects of this study have been presented elsewhere<sup>9,12</sup>). This combination of experimental and theoretical methods provides a self-consistent unified view of the spin density distribution within the dithiadiazolyl ring. The results are not only useful for future studies in dithiadiazolyl radical chemistry but the information (especially with regard to the radial extension of the spin density at the heavier  $p$ -block element) is of fundamental importance for the construction of future molecule-based magnets.

**II. EXPERIMENTAL SECTION****A. Synthesis**

The synthesis of aryl-substituted-1,2,3,5-dithiadiazolyl radicals is conveniently carried out *via* condensation of an amidine or silylated amidine with SCl<sub>2</sub>, followed by reduction with Ph<sub>3</sub>Sb, Ag powder or Zn/Cu couple. This approach became widely used after a report by Oakley who described a general synthetic route to silylated amidinate salts from aromatic nitriles.<sup>13</sup> In our current studies, the parent nitrile,  $p$ -O<sub>2</sub>NC<sub>6</sub>F<sub>4</sub>CN (**1**) was not commercially available. The amine  $p$ -H<sub>2</sub>NC<sub>6</sub>F<sub>4</sub>CN appeared a plausible precursor to **1**, although the electron-withdrawing nature of the perfluoroaromatic ring made the amine group particularly resilient to oxidation. Eventually we found that urea-H<sub>2</sub>O<sub>2</sub> with trifluoroacetic anhydride, which acts as a convenient source of the

strong oxidizing agent trifluoroperacetic acid,  $\text{CF}_3\text{C}(=\text{O})\text{OOH}$ , afforded **1** in moderate yields (39%). This oxidizing mixture has been utilized previously by Heaney *et al.*<sup>14</sup> Conversion of **1** into the dithiadiazolyl radical  $p\text{-O}_2\text{NC}_6\text{F}_4\text{CNSSN}$  (**2**) followed normal synthetic procedures. Radical **2** was isolated as a crystalline solid in 16% yield (for the three-step synthesis from **1**) by vacuum sublimation. The preliminary x-ray and magnetic studies of **2** have been reported in a previous communication.<sup>11</sup> Large single crystals for the work described here were prepared by annealing a small sample (approximately 60 mg) in a sealed tube under  $\text{N}_2$  for 3–4 hours at 100 °C. While there was evidence for some decomposition (formation of an intrac-table brown oil on the surface of the glass), a small number of large single crystals were also formed with upper dimensions in the region  $1 \times 1 \times 1 \text{ mm}^3$ .

### B. Single-crystal nonpolarized neutron diffraction

A single crystal of **2** of dimensions  $1 \times 1 \times 1 \text{ mm}^3$  was mounted in an Air Products 512 Displex cryostat on the four-circle diffractometer D9 at the Institut Laue Lagevin (ILL), and cooled down to 20 K. A total of 3278  $\omega$  scans of Bragg peaks extending to  $\sin \theta/\lambda = 0.59 \text{ \AA}^{-1}$  were collected with a small area detector at a calibrated wavelength of  $0.8339(1) \text{ \AA}$ , from a Cu[220] monochromator. After merging, 1281 independent reflections were obtained. The unit-cell parameters obtained from the observed centroids of the 788 stronger reflections are  $a=b=8.1052(2) \text{ \AA}$ ,  $c=14.7616(6) \text{ \AA}$ , and  $\alpha=\beta=\gamma=90^\circ$ . The integrated intensities were corrected for absorption using the Gaussian integration method and the calculated linear absorption coefficient  $\mu=0.0213 \text{ mm}^{-1}$ . The integrated intensities were also corrected for multiple scattering although the nearly insignificant intensities of the systematically absent reflections indicate that this effect is not important.

Atom positions, anisotropic displacement parameters, and the mosaicity for the extinction correction were refined using the SFLSQ program of the CCSL suite.<sup>15</sup> The parameters were optimized against the square of the structure factor amplitudes  $|F_N^2|$  with  $1/\sigma^2$  as weight of the reflections, where  $\sigma$  is the standard deviation of the reflection intensity. The scattering lengths for S, F, O, N, and C were 0.2847, 0.5654, 0.5805, 0.936, and  $0.6646 \times 10^{-12} \text{ cm}$ , respectively.<sup>16</sup> The least-squares refinement converged with the following agreement factors:  $R=0.037$ ,  $R_w=0.026$ , and  $\chi^2=3.31$ .

### C. Single-crystal polarized neutron diffraction

A polarized neutron-diffraction experiment was undertaken on the D3 lifting-counter diffractometer at the ILL. The same crystal of **2** which was used in the nonpolarized neutron-diffraction experiment was placed in a cryomagnet and cooled to 1.5 K. A Heusler crystal was used to monochromate the incoming neutron beam at a wavelength of  $0.843 \text{ \AA}$ , with a polarization of 0.93. A cryoflipper, with an efficiency of 1.00, changed the polarization between parallel and antiparallel relative to the vertical magnetic field of 9 T applied to the sample. Despite the data collection extending over 22 days, flipping ratios for only one crystal orientation

could be measured because of the low magnetization density and the small crystal size ( $1 \text{ mm}^3$ ). The crystal was mounted with the  $c$  axis perpendicular to the magnetic field. This is the orientation, due to the symmetry of the crystal, which maximizes the number of accessible independent reflections. A total of 296 flipping ratios were measured out to  $\sin \theta/\lambda = 0.72 \text{ \AA}^{-1}$  which yielded 128 independent ratios after merging over repeated and symmetry-equivalent reflections.

### D. X-ray experiment

A  $0.1 \times 0.1 \times 0.1 \text{ mm}^3$  single crystal of **2** was mounted on a Bruker SMART-6000 CCD diffractometer equipped with an Oxford Cryosystems Cryostream nitrogen-flow cooling device.<sup>17</sup> Diffraction data were collected at 100 K, using graphite-monochromated Mo  $K\alpha$  radiation,  $\lambda=0.71073 \text{ \AA}$ . Data were collected in three 900-frame  $\omega$  scans ( $\phi=0^\circ, 120^\circ, 240^\circ$ ) at each of three different area-detector positions ( $2\theta=-25^\circ, -60^\circ$ , and  $-90^\circ$ ), producing a total of 8100 frames sampled at intervals of  $0.2^\circ$  in  $\omega$ . Cell parameters were refined using the SMART software<sup>18</sup> and raw frame data were integrated using the SAINT program.<sup>19</sup> The reflection intensities were corrected for absorption by numerical integration based on measurements and indexing of the crystal faces using SHELXTL software<sup>20</sup> ( $\mu=0.60 \text{ mm}^{-1}$ ). A total of 72 295 reflections were measured in the range  $-20 < h < 20$ ;  $-19 < k < 20$ ;  $-37 < l < 36$ , up to a resolution of  $(\sin \theta/\lambda)_{\text{max}}=1.25 \text{ \AA}^{-1}$  ( $2\theta=125^\circ$ ). From these, 4162 unique reflections with  $F_{\text{obs}} > 3\sigma(F_{\text{obs}})$  and  $(\sin \theta/\lambda) \leq 1.04 \text{ \AA}^{-1}$  were used for the structure refinement, as data above  $1.04 \text{ \AA}^{-1}$  were too weak to contain any structural information. The structure was refined with anisotropic displacement parameters for all the atoms by full-matrix least-squares methods with the SHELXTL program. The Flack parameter<sup>21</sup> of 0.02(3) indicates that we have chosen the correct absolute structure.

### E. EPR and ENDOR experiments

For solution EPR studies, a small quantity of **2** was dissolved in tetrahydrofuran (THF/ $d^8$ ) toluene. Frozen solution EPR and ENDOR spectra were recorded on  $\text{CD}_2\text{Cl}_2$  solutions containing a few drops of  $d^8$  toluene to improve the glass. All the solvents were fully deuterated. The  $X$ - and  $Q$ -band EPR and ENDOR spectra were recorded on a cw Bruker ESP 300E series spectrometer equipped with an ESP360 DICE ENDOR unit, operating at 12.5 kHz field modulation. The  $X$ -band EPR/ENDOR measurements were performed in a Bruker EN801 ENDOR cavity while the  $Q$ -band EPR/ENDOR measurements were performed in a Bruker ER5106QT resonator. The ENDOR spectra were obtained at 10 K using 8 dB rf power from an ENI A-300 rf amplifier, with 50 kHz rf modulation depth and 200  $\mu\text{W}$  power at  $X$  band, and using 12 dB rf power from a 3200L rf amplifier, 250 kHz rf modulation depth and 150 W power at  $Q$  band. Accurate  $g$  values were obtained using a Bruker ER 035 M NMR Gaussmeter calibrated using the perylene radical cation in conc.  $\text{H}_2\text{SO}_4$ ,  $g=2.002569$ . Accurate frequencies at  $Q$  band were determined using an Agilent 53152A frequency counter. The ENDOR spectra were simulated us-

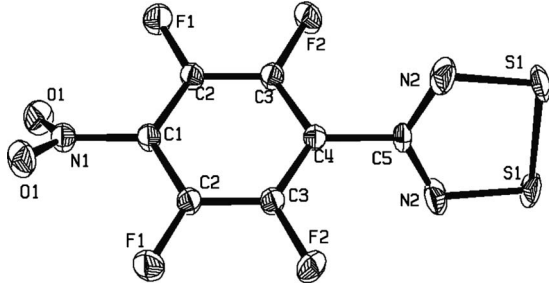


FIG. 1. Molecular structure of **2** at 20 K determined by single-crystal neutron diffraction. Displacement ellipsoids are shown at the 99% probability.

ing an in-house programme based on the resonance expressions of Hurst *et al.*, for ENDOR resonances in disordered systems. The full expression given by Hurst *et al.*,<sup>22</sup> which calculates the resonant frequencies for the ENDOR transitions is given by

$$h\nu = \left[ \sum_{i=1}^3 \left[ \frac{m_s}{g(\theta, \phi)} \left( \sum_{j=1}^3 g_j l_j A_{ji} \right) - l_i \nu_N \right]^2 \right]^{1/2}, \quad (1)$$

where  $l_{ij}$  represents the direction cosines for the applied magnetic field vector and the other symbols have their usual meaning.

### III. ANALYSIS AND RESULTS

#### A. Determination of the low-temperature crystal structure through neutron diffraction

The x-ray crystal structure of **2** at 220 K has been reported previously.<sup>11</sup> This radical crystallizes in the noncentrosymmetric tetragonal space group  $P4_12_22$ , with half a molecule in the asymmetric unit and four molecules per unit cell. In order to determine accurately the atomic positions, thermal displacement parameters and extinction parameters which are required for the extraction of magnetic structure factors from the flipping ratios from the low-temperature polarized neutron-diffraction (PND) experiment (*vide infra*), an unpolarized neutron-diffraction experiment was performed on the four-circle diffractometer D9 of the Institut Laue Langevin (ILL) in Grenoble, France, at 20 K. The molecular structure of **2**, which is supplied as supplementary material, is presented in Figure 1.

Moreover, an additional x-ray experiment at 100 K was also performed in order to follow the evolution of the structure with temperature by comparing the x-ray structures at 220 and 100 K and the neutron-diffraction structure at 20 K.

#### B. Spin density distribution from polarized neutron diffraction

The magnetization density is the Fourier transform of the magnetic structure factors  $F_M$ , which can be experimentally determined by the PND technique. In the paramagnetic regime, there is no spontaneous magnetization in the sample and magnetic saturation is achieved by the application of a large magnetic field at low temperature (in order to minimize

thermal fluctuations of the electron spins). In **2**, magnetic saturation of the sample was achieved by the application of a 9 T magnetic field at 1.5 K, just above the ferromagnetic ordering temperature (1.3 K).

While the nuclear contribution to the diffraction intensities is independent of the polarization of the neutron beam, the magnetic contribution varies depending on whether the incident beam is polarized parallel or antiparallel to the applied field. In a PND experiment, the measured quantity is the flipping ratio  $R = I^+ / I^-$ , where  $I^+$  and  $I^-$  are the diffracted intensities with the incident neutron beam polarization parallel and antiparallel, respectively, to the applied magnetic field.  $R$  is given by

$$R(\mathbf{h}) = \frac{I^+}{I^-} = \frac{|F_N|^2 + 2pq^2(F'_N F'_M + F''_N F''_M) + q^2 |F_M|^2}{|F_N|^2 - 2epq^2(F'_N F'_M + F''_N F''_M) + q^2 |F_M|^2}, \quad (2)$$

where  $\mathbf{h}$  is the scattering vector of the Bragg reflection,  $F_N$  and  $F_M$  are the nuclear and magnetic structure factors, respectively,  $q$  is the sine of the angle between the scattering vector and the magnetic field direction,  $p$  is the polarization of the incident beam, and  $e$  is the flipping efficiency. When the crystal structure is noncentrosymmetric, as in the present case, both the magnetic structure factors and the nuclear structure factors are complex,  $F_N = F'_N + iF''_N$  and  $F_M = F'_M + iF''_M$ , and the magnetic structure factors cannot be directly extracted from Eq. (2). Instead, the spin density has been modeled to provide a best fit to the flipping ratios. Two approaches have been utilized to model the spin density distribution; (a) a magnetic wave-function approach<sup>23</sup> and (b) a multipolar-expansion approach,<sup>24</sup> in both cases using a modification of the program MOLLY.<sup>25</sup>

The reference coordinate system used for both approaches is the same for all the atoms in the heterocyclic ring with the  $z$  axis perpendicular to the ring plane and the  $x$  axis parallel to the twofold symmetry axis of the molecule.

The limited number of data forced us to apply several constraints to the models in order to avoid overparameterization. Previous *ab initio* DFT calculations and EPR studies on related dithiadiazolyl derivatives have indicated that the spin density on the dithiadiazolyl ring substituent is negligible.<sup>26</sup> Therefore, in both approaches, only the atoms in the heterocyclic ring have been considered. The appropriateness of the assumption of no spin density in the atoms not in the heterocyclic ring is reflected in the good agreement factors between the fits and the data ( $\chi^2 = 2.33$  for nine variables in the wave-function approach and  $\chi^2 = 1.28$  for 25 variables in the multipolar expansion).

#### 1. Magnetic wave-function approach

In this approach, the spin density  $S(\mathbf{r})$  is expanded as

$$S(\mathbf{r}) = \sum_i S_i \langle \psi_i | \psi_i \rangle, \quad (3)$$

where  $i$  labels the atoms included in the refinement. The  $S_i$  are the atomic spin populations and the  $\psi_i$  are the atomic magnetic wave functions, which are linear combinations of standard Slater atomic orbitals,

TABLE I. Slater radial exponents ( $\xi$ ), spin populations ( $S_i$ ), and  $\alpha_{ij}$  coefficients in the refinement of the spin density utilizing the wave-function approach.

	S1	N2	C5
$S_i$	0.301(1)	0.222(1)	-0.046(1)
$\xi$	2.05	1.95	1.72
$\alpha_{ij}$			
$p_z$	0.996(05)	0.910(09)	1.0
$p_x$	-0.034(10)	0.319(17)	
$p_y$	-0.078(15)	-0.225(23)	
$2s$		-0.135(04)	

$$\psi_i = \sum_j \alpha_{ij} \varphi_j, \quad (4)$$

where the parameters,  $\alpha_{ij}$ , fulfill the condition  $\sum_j |\alpha_{ij}|^2 = 1$ . The atomic spin populations,  $S_i$ , the parameters,  $\alpha_{ij}$ , and the radial exponents of the Slater atomic orbitals are the parameters of the model. In order to reduce further the number of parameters, the minimum number of orbitals required to model the spin density was employed. Preliminary models showed that the spin density distribution was of  $\pi$ -type character with the population on the C site being an order of magnitude lower than those on the S and N sites. As a consequence, the model only included a  $2p_z$  orbital for the carbon atom. The larger spin densities on N and S justified the inclusion of additional orbitals to model the data accurately. For nitrogen, the geometry [ $\angle \text{CNS} = 113.25^\circ(9)$ ] can be considered close to  $sp^2$  hybridization and the  $2s$  orbital was included in addition to the  $2p_x$ ,  $2p_y$ , and  $2p_z$  orbitals. As for the sulfur atom [ $\angle \text{NSS} = 94.67^\circ(5)$ ], no hybridization between the  $3s$  and  $3p$  orbitals is expected, and therefore only the  $3p_x$ ,  $3p_y$ , and  $3p_z$  orbitals were considered in order to not increase the number of free parameters. The radial exponents of the Slater atomic orbitals  $\xi$  were fixed in order to avoid an unphysical increase in the radial exponent of the nitrogen

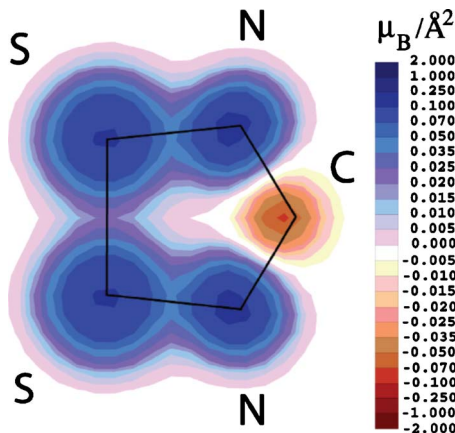


FIG. 2. (Color online) Projection of the calculated spin density distribution in one molecule onto the plane containing the dithiadiazolyl ring using the wave-function approach.

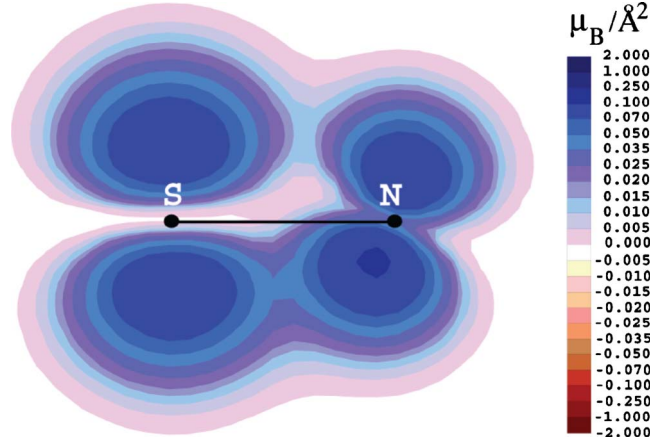


FIG. 3. (Color online) Projection of the calculated spin density distribution of the sulfur and nitrogen atoms of one side of the dithiadiazolyl ring in a plane perpendicular to the dithiadiazolyl ring and perpendicular to the molecular twofold axis using the wave-function approach.

atom due to a high correlation observed in initial refinements between this parameter and the nitrogen and carbon spin populations. These fixed  $\xi$  values were taken from Fitzpatrick and Murphy,<sup>27</sup> where self-consistent-field molecular calculations had been performed in order to obtain standard  $\xi$  values for atoms in molecules.

The saturation magnetization,  $M_{sat}$ , for an  $S=1/2$  system such as **2** is  $2S\mu_B$  per radical, i.e.,  $1\mu_B$ . The spin population, normalized to  $1\mu_B$  per radical, and the  $\alpha_{ij}$  coefficients are listed in Table I. Figures 2 and 3 illustrate the spin density distribution within, and perpendicular to, the dithiadiazolyl ring plane using this wave-function approach.

## 2. Multipolar expansion approach

In this approach, the spin density is partitioned into separate atomic contributions which are expanded in the basis of real spherical harmonics  $d_{lm}$ , which are also referred to as multipoles,<sup>24</sup>

$$m(\mathbf{r}) = \sum_{i \in \text{atoms}} \sum_l R_i^{l,dens}(|\mathbf{r} - \mathbf{r}_i|) \sum_{m=-l}^{m=l} P_{ilm} d_{lm}(\theta_i, \varphi_i), \quad (5)$$

where  $P_{ilm}$  are the population coefficients of the real spherical harmonics  $d_{lm}(\theta_i, \varphi_i)$  and  $R_i^{l,dens}$  are Slater radial functions. In order to minimize the number of parameters, the Slater radial exponents  $\zeta$ , together with the  $n_l$  values of the Slater radial functions were determined from atomic Slater exponents  $\xi$  taken from the literature,<sup>27</sup> using the relation  $\zeta$

TABLE II. Slater radial exponents and spin populations determined within the framework of the multipolar-expansion approach.

	S1	N2	C5
Spin pop.	0.282(1)	0.245(1)	-0.057(1)
$\zeta$	4.10	3.90	3.44
$n_l$	4	2	2

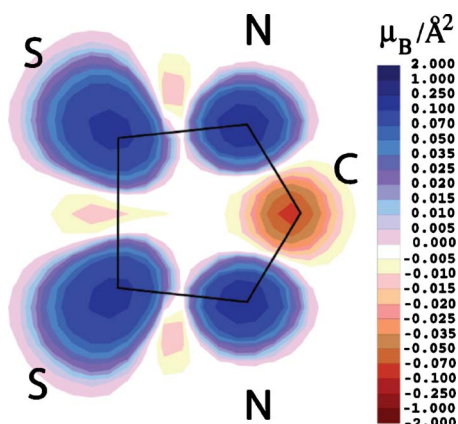


FIG. 4. (Color online) Projection of the calculated spin density distribution in one molecule onto the plane containing the dithiadiazolyl ring using the multipolar-expansion approach.

$=2\xi$ . Since the spin density arises from  $s$  and  $p$  orbital contributions,  $l=0$  and  $1$ , respectively, the model included a multipolar expansion up to order 2 ( $2l_{max}$ ) for the sulfur, nitrogen, and carbon atoms. The spin populations thus obtained, normalized to  $1\mu_B$  per radical, are listed in Table II. Figures 4 and 5 illustrate the spin density distribution in, and perpendicular to, the dithiadiazolyl ring plane, using the multipolar-expansion approach.

### C. Density-functional theory calculations

Density-functional theory has been proven to give excellent results in the computation of the spin populations for organic radicals,<sup>28,29</sup> allowing the comparison with experimental spin populations determined by EPR and/or polarized neutron-diffraction studies. In the DFT computations, the geometry of **2** was fixed to the nuclear structure obtained from the low-temperature nonpolarized neutron experiment. Computations were performed using the DMOL3 package<sup>30</sup> on

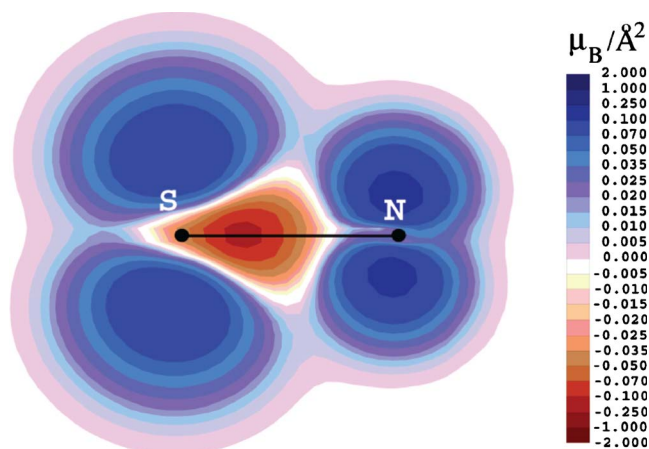


FIG. 5. (Color online) Projection of the calculated spin density distribution of the sulfur and nitrogen atoms of one side of the dithiadiazolyl ring in a plane perpendicular to the dithiadiazolyl ring and perpendicular to the molecular twofold axis using the multipolar-expansion approach.

TABLE III. Mulliken atomic spin populations for **2** determined by DFT methods.

Atom	Periodic	Molecular
S1	0.320	0.311
N2	0.213	0.224
C5	-0.063	-0.065
C4	0.005	0.005
C3	-0.003	-0.004
C2	0.002	0.001
C1	-0.003	-0.003
F2	0.000	0.000
F1	0.000	0.000
N1	0.001	0.000
O1	0.000	0.000

both the periodic system and on the isolated radical, in order to inspect the influence of the environment on the radical. The calculations were performed using the Perdew-Wang91 exchange-correlation functional<sup>31</sup> and an atom-centered double-numeric polarized basis set. In this basis set, which is the most complete one available within the DMOL3 package, each valence orbital is parameterized by two numerical wave functions and polarization wave functions are also included. These all-electron calculations were carried out over the “fine” numerical integration grid and with a multipolar expansion of the electron density on all the atoms up to the octupole order. The self-consistent-field threshold was set to  $10^{-8}$  a.u. An additional set of calculations performed using the 220 K x-ray structural data produced no significant differences in the spin density distribution. The Mulliken spin populations for both the periodic and the molecular calculations are listed in Table III. Figure 6 represents two spin density isosurfaces, one negative and the other positive, from the molecular DMOL3 Perdew-Wang91 calculation.

### D. EPR spectroscopy

Room-temperature X-band EPR spectra of **2** in THF solution exhibit a well-defined isotropic quintet of triplets consistent with coupling of the unpaired electron to the two equivalent N atoms and the two F atoms in the *ortho* position to the dithiadiazolyl ring ( $g=2.01$ ,  $a_N=5.2$  G, and  $a_F=1.3$  G). The  $g$  value and N hyperfine interactions are simi-

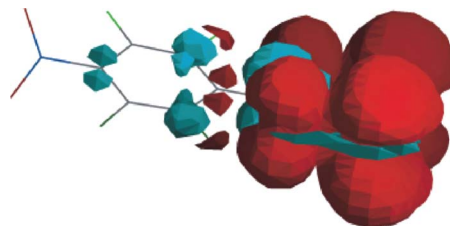


FIG. 6. (Color online) Spin density isosurfaces of **2** determined from a DFT Perdew-Wang 91 calculation. Red (dark) isosurface:  $2 \times 10^{-4} \mu_B/\text{\AA}^3$ ; blue (light) isosurface:  $-2 \times 10^{-4} \mu_B/\text{\AA}^3$

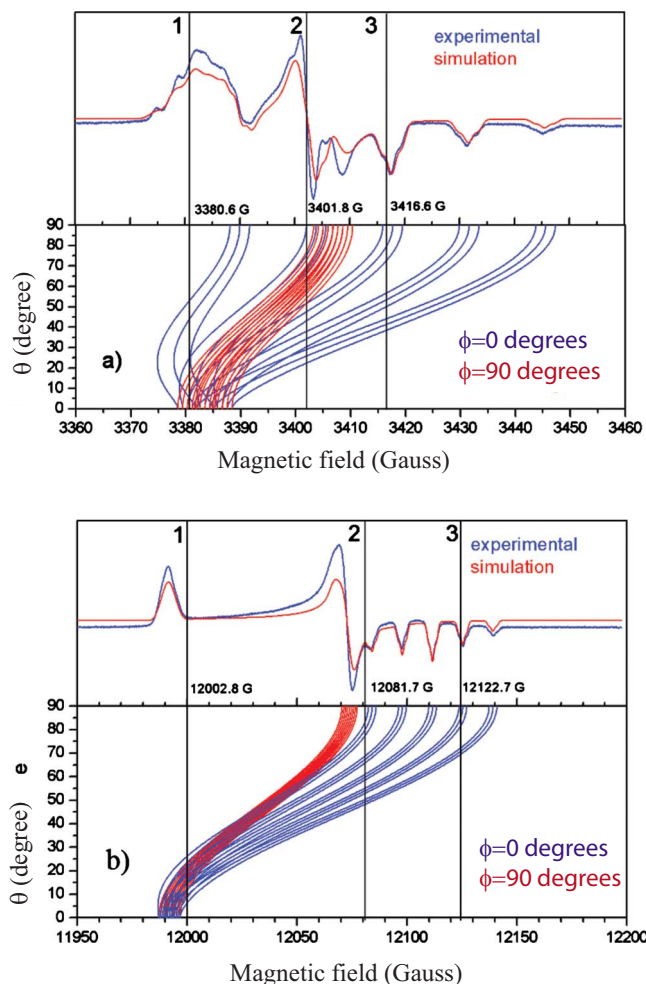


FIG. 7. (Color online) Experimental and simulated EPR spectra of **2** recorded at (a) X-band frequencies at 106 K (upper spectrum); and (b) Q-band frequencies at 10 K (lower spectrum). The angular dependence of the resonance positions for both spectra is illustrated.

lar to those observed for other 1,2,3,5-dithiadiazolyl radicals.<sup>32</sup> The additional fluorine hyperfine interaction is of a similar order to that previously reported for  $C_6F_5CNSSN$ ,  $p\text{-Br}C_6F_4CNSSN$ , and  $p\text{-NCC}_6F_4CNSSN$ .<sup>26</sup> Frozen solutions of **2** in deuterio-toluene at X band reveal a rhombic symmetry in the  $g$  tensor ( $g_1 \neq g_2 \neq g_3$ ) with a well-resolved N hyperfine interaction to the  $g_3$  component and with some additional evidence of a fluorine hyperfine interaction, although this was not well resolved. A plot of the angular dependencies of the hyperfine interaction and  $g$  tensor at X band has

led to the observation of undershoot resonances (off-axis turning points) which might cause some spectral misassignment in the ENDOR analysis (*vide infra*). These angular anomalies are quite common in X-band powder spectra when the A anisotropy is large; at Q-band frequency the  $g$  anisotropy dominates the spectrum so the anomaly does not occur. Therefore, in order to avoid this problem, additional EPR spectra of **2** were recorded at Q-band frequencies (33.9905 GHz). Subsequent simulation of both X- and Q-band EPR spectra with the same set of parameters allowed their angular dependencies to be unambiguously determined. The X- and Q-band EPR spectra with their simulations and angular dependencies are shown in Figs. 7(a) and 7(b), respectively. The fitting parameters are given in Table IV. Some inaccuracies in the anisotropic  $^{14}N$  and  $^{19}F$  hyperfine couplings to  $g_2$  and  $g_3$  components arise because the couplings are less than the inherent linewidth of the spectrum. The values quoted are upper limits to these interactions. The signs of  $^{14}N$  and  $^{19}F$  hyperfine interactions cannot be unambiguously determined. Nevertheless the average of the anisotropic components should closely resemble the isotropic value measured in solution. In order to obtain good agreement between the average values  $\langle a_N \rangle$  and  $\langle a_F \rangle$  and the isotropic values, the signs of the two smallest hyperfine interactions, i.e.,  $a_2^N$  and  $a_3^N$ , must be opposite.

### E. ENDOR spin populations

Room-temperature X-band EPR spectra of **2** in  $CD_2Cl_2/Tol\text{-}d_8$  solution exhibit a well-defined isotropic quintet of triplets consistent with coupling of the unpaired electron to the two equivalent N atoms and the two F atoms in the *ortho* position to the dithiadiazolyl ring ( $g_{iso} = 2.01, a_N = 5 \text{ G}, a_F = 1.7 \text{ G}$ ). A typical quasiisotropic EPR spectrum is shown in Figure 8. Attempts were made to measure the solution ENDOR spectra over a range of temperatures in order to extract the isotropic couplings. Despite a range of temperatures and rf/MW powers, we were unable to detect the solution ENDOR resonances due to unfavorable nuclear and electron relaxation rates in the cw experiment.

In order to determine the anisotropy in the F-hyperfine spectra and to extract a more reliable estimate of the magnitude of the F couplings to both the *ortho*-fluorine and also to the metafluorines (which do not exhibit any resolved hyperfine coupling in the cw-EPR experiments), additional low-temperature ENDOR studies were undertaken at both X- and Q-band frequencies.

Figure 9 reflects the effect of the magnetic field on the electron spin (the electron-Zeeman interaction), the effect of

TABLE IV. Anisotropic and isotropic EPR spin-Hamiltonian parameters for **2** determined by simulation of the frozen solution and liquid EPR spectra at X-band and Q-band frequencies. Field given in gauss (G).

	$g$ tensor	N-hfine	G	MHz	Ortho-F-hfine	G	MHz
$g_1$	2.0016	$a_1^N$	13.9	39	$a_1^F$	3.2	9
$g_2$	2.00795	$a_2^N$	$\pm 0.9$	$\pm 2.5$	$a_2^F$	$\pm 1.8$	$\pm 5$
$g_3$	2.0218	$a_3^N$	$\pm 0.9$	$\pm 2.5$	$a_3^F$	$\pm 1.8$	$\pm 5$
$\langle g \rangle$	2.01045	$\langle a_N \rangle$	5.2	14.6	$\langle a_F \rangle$	1.07	3.0
$g_{iso}$	2.0118	$a_{iso}^N$	5.2	14.6	$a_{iso}^F$	1.3	3.6

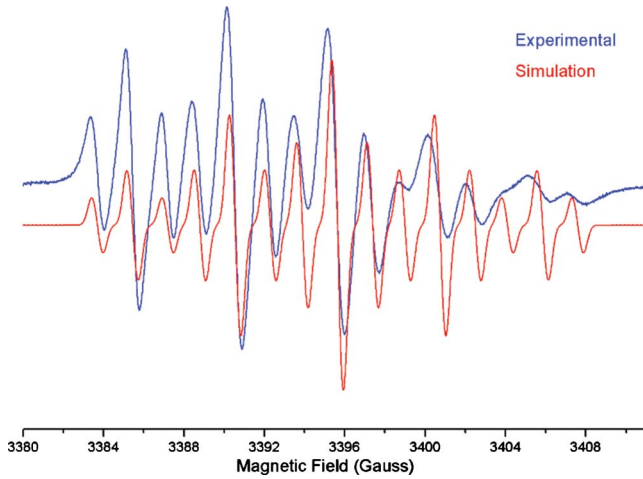


FIG. 8. (Color online) Quasi-isotropic EPR experiment.

the magnetic field on the nuclear spin (nuclear-Zeeman term), and the effect of the electron-nuclear interaction for a system coupling to two chemically equivalent  $^{19}\text{F}$  ( $I=1/2$ ) atoms. The energies (in frequency units) of the different resultant spin states are a function of  $M_s$ ,  $M_{I(F1)}$ , and  $M_{I(F2)}$ ,

$$E(M_s, M_{I(F1)}, M_{I(F2)}) = g\mu_B H M_s - g\mu_n H M_I + h a M_s M_I. \quad (6)$$

The addition of further interactions to the assumed two  $^{19}\text{F}$  atoms and two  $^{14}\text{N}$  atoms complicates the energy-level manifold but the following discussions of the transitions observed in the EPR and ENDOR experiments are essentially the same. In the conventional EPR experiment, a fixed microwave (MW) frequency is applied to the sample and the magnetic field is swept in order to observe the resonance between  $M_s = -1/2$  and  $M_s = +1/2$  electron-spin states. The allowed

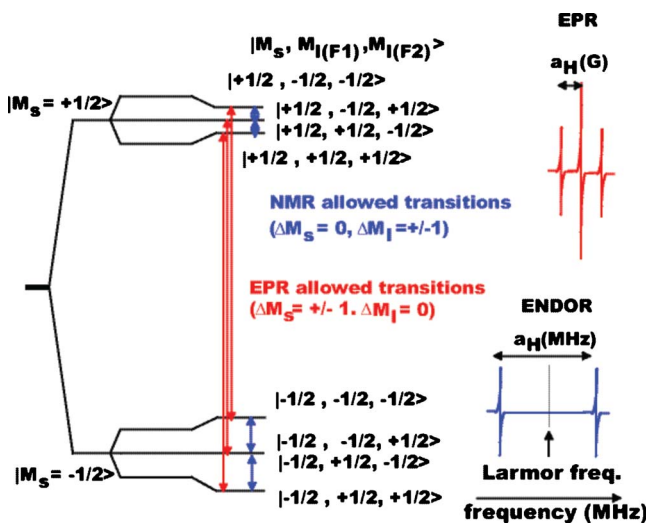


FIG. 9. (Color online) Energy-level diagram for the interaction of an electron spin ( $S=1/2$ ) with two equivalent nuclei ( $I=1/2$ ) in the presence of an applied magnetic field. Allowed EPR and ENDOR (NMR) transitions are labeled in red (long arrows) and blue (short arrows), respectively.

EPR transitions,  $\Delta M_I = 0$  and  $\Delta M_S = \pm 1$ , are shown in Figure 9. Small hyperfine couplings may often be lost in the line-width of the EPR spectrum. Such small, unresolved couplings may be detected in double-resonance experiments such as ENDOR. In the ENDOR experiment, both the applied field and the microwave frequency remain fixed and the radiofrequency region is swept. Absorption then occurs according to the NMR selection rules  $\Delta M_I = \pm 1$  and  $\Delta M_S = 0$ . In the isotropic  $I=1/2$  case (assuming  $\nu_n > a/2$ ), this leads to a pair of absorption lines centered about the nuclear Larmor frequency ( $\nu_n$ ) for the particular nucleus (E) with separation  $a_E$ . This not only allows very small hyperfine couplings to be measured directly but also allows the type of nucleus to be assigned unambiguously. For a randomly oriented polycrystalline sample, the interpretation becomes substantially more complex and is usually achieved by simulation.

ENDOR studies on **2** at both  $X$  and  $Q$  band were recorded at positions close to the principal  $g$  values (e.g., positions 1, 2, and 3, marked in Fig. 7) corresponding to the principle turning points in the spectra. The  $X$ -band ENDOR spectra were however complicated by the powder-type ENDOR profiles observed at each field position (marked 1, 2, and 3 in Fig. 7(a) corresponding to the fields 3380.6, 3401.8, and 3416.6 G]. A large set of angles was effectively selected at positions 1 and 2, due to the off-axis turning point (at 3380.6 G) and the wide range of orientations at 3401.8 G due to overlapping contributions from  $g_2$  and  $g_3$  components. In principal, a single-crystal-type ENDOR spectrum could have been observed at the highest field position (3445 G) but the resulting cw-ENDOR intensity was too low for accurate analysis. At position 2, the spectra were sufficiently strong but once again complicated by the number of angles selected in the ENDOR measurements. For these reasons, the ENDOR spectra were recorded and analyzed in depth at the higher frequency ( $Q$  band). Owing to the improved resolution in the  $g$  tensor and the absence of the angular anomaly, the powder-type ENDOR spectra measured at  $Q$  band were easier to simulate owing to the reduced number of angles selected at the field positions 1, 2, and 3 [see angular  $Q$ -band dependency plot in Fig. 7(b)]. The ENDOR studies clearly reveal two chemically distinct  $^{19}\text{F}$  atoms; one with a relatively large hyperfine coupling which is resolved in the EPR spectra and a second with substantially smaller coupling which cannot be detected in the conventional cw-EPR studies (Table V). A representative  $Q$ -band ENDOR spectra measured at the field 12081.7 G is presented in Fig. 10, together with the associated simulation.

It is noteworthy that the hyperfine matrices of the fluorine atoms are not collinear with the  $g$  matrix. Nevertheless, the noncoincidence of hyperfine and  $g$ -tensor matrices is unlikely to have a marked effect on the EPR spectrum because of the low magnitude of the F hyperfine interaction. This noncoincidence is likely to manifest itself in some asymmetry in the line shape. While the anisotropy in the *ortho*-F appears axial, it is clearly rhombic in the case of the *meta*-F. Given the rhombic anisotropy of the molecule (reflected in its  $g$ -tensor anisotropy), the axial symmetry of F(1) would appear entirely fortuitous. The cw-EPR studies indicated that  $A_1$  and  $A_2$  interactions should be of opposite sign in order to provide good agreement with the isotropic values. The

TABLE V. Anisotropic and isotropic EPR spin-Hamiltonian parameters for **2** determined by simulation of the frozen solution and liquid EPR spectra at X-band and Q-band frequencies. Field given in gauss (G).

Hyperfine couplings					
Nucleus	Linewidth	$A_1$ (MHz)	$A_2$ (MHz)	$A_3$ (MHz)	$\langle a \rangle$ (MHz)
<i>Ortho</i> -F	1	$\pm 3.5$	$\pm 3.5$	11.4	3.8
<i>Meta</i> -F	0.13	$\pm 0.4$	$\pm 0.19$	1.0	
Euler angles (deg)					
Nucleus	$\alpha$	$\beta$	$\gamma$		
<i>Ortho</i> -F	90	28	0		
<i>Meta</i> -F	15	90	0		

much-improved resolution of these hyperfine couplings now provides much better agreement with the isotropic interactions to the *ortho*-F (Tables IV and V). In addition, the previously unresolved hyperfine coupling to the *meta*-F can now be determined. However, the absence of an experimentally determined isotropic hyperfine coupling to the *meta*-F precludes a determination of the relative signs of the anisotropic couplings to this nucleus. These are an order of magnitude less than the hyperfine interaction to the *ortho*-F.

#### IV. DISCUSSION

##### A. Structural studies

The structure of **2** has now been determined at three different temperatures. The original single-crystal study was measured at 220 K,<sup>11</sup> an x-ray structure resolution was performed at 100 K and the nonpolarized neutron-diffraction study was determined at 20 K. An examination of the bond lengths and angles within **2** revealed negligible changes on cooling. The heterocyclic bond distances and angles are in

good agreement with those reported for other dithiadiazolyl radical structures.<sup>2</sup> The C—N bond at 1.3308(6) Å is intermediate between values expected for C—N single and C=N double bonds (1.47 and 1.27 Å, respectively).<sup>33</sup> However, there is a contraction of the unit-cell volume by 2.5% on cooling from 220 to 20 K (Table VI). While there is some small contraction of the *a* axis (and equivalent *b* axis) on cooling from 220 to 100 K, there is little further change (within 3 esd's) on further cooling to 20 K. Molecules are linked within the *ab* plane along the (110) direction via S···O contacts which are strongly electrostatic in nature. These contacts are less than the sum of the van der Waals radii and contraction of the lattice in the *ab* plane is likely to lead to destabilizing short-range repulsive interactions. The small change in this intermolecular contact is reminiscent of that present in the  $\beta$  phase of *p*-NCC<sub>6</sub>F<sub>4</sub>CN<sub>2</sub>SSN which also exhibits a resilience to cell contraction along its crystallo-

TABLE VI. Temperature dependence of unit cell and selected structural parameters for **2**.  $\theta$  is the angle between CN<sub>2</sub>S<sub>2</sub> and C<sub>6</sub>F<sub>4</sub> mean planes and  $\psi$  the angles between O<sub>2</sub>N and C<sub>6</sub>F<sub>4</sub> mean planes.

	20 K	100 K	220 K
<i>a</i> (Å)	8.1052(2)	8.1101(1)	8.1380(4)
<i>c</i> (Å)	14.7616(6)	14.8415(2)	15.0490(12)
<i>V</i> (Å <sup>3</sup> )	969.75(6)	976.18(3)	996.65(11)
<i>D<sub>c</sub></i> (g/cm <sup>3</sup> )	2.042	2.027	1.987
Bonds (Å) and angles (deg) within CN <sub>2</sub> S <sub>2</sub>			
C—N	1.333(1)	1.3308(6)	1.325(2)
N—S	1.639(2)	1.6379(5)	1.635(2)
S—S	2.088(4)	2.0894(3)	2.081(1)
∠NCN	124.14(10)	123.83(11)	123.9(3)
∠CNS	113.25(9)	113.56(05)	113.5(2)
∠NSS	94.67(5)	94.52(02)	94.5(1)
$\theta$	56.34	56.92	57.75
$\psi$	42.94	43.01	43.63
Intermolecular contacts (Å)			
N···S	3.600(2)	3.6569(4)	3.681(5)
S···O	3.186(2)	3.1934(5)	3.228(4)

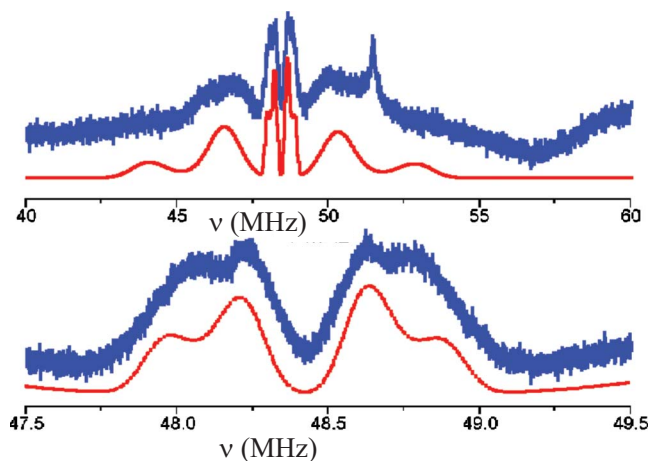


FIG. 10. (Color online) Experimental Q-band ENDOR spectrum (10 K) and associated simulation of **2** measured at the static magnetic field positions of 12081.7 G. The wide and narrow sweeps <sup>19</sup>F ENDOR spectra are shown.

graphic *c* axis (along which electrostatically favorable CN $\cdots$ S interactions propagate).<sup>7</sup> Instead, in **2**, the expected contraction of the unit cell upon cooling is predominantly accommodated by a shortening of the crystallographic *c* axis (1.9% from 220 to 20 K). This contraction of the *c* axis is accommodated by a small decrease in the twist angle between the dithiadiazolyl ring and the perfluorophenyl ring.

The dihedral angle between the mean plane defined by the NO<sub>2</sub> group and the one defined by the perfluorophenyl ring also changes. These small adjustments of the molecular torsion angles lead to some small changes in the intermolecular contacts. Perhaps the most important of these are the S $\cdots$ N contacts; each molecule forms four symmetry equivalent contacts of this type. We have previously proposed<sup>11</sup> that these S $\cdots$ N contacts form the magnetic-exchange pathways, and generate the three-dimensional network of interactions necessary for bulk magnetic order in a Heisenberg-type system. The temperature dependence of selected intramolecular, intermolecular, and crystallographic parameters are presented in Table VI.

### B. Polarized neutron diffraction

The results of the PND studies using both wave-function and multipolar-expansion approaches are in close agreement. They indicate that the spin density is almost entirely localized in  $p_z$  orbitals of the nitrogen and sulfur atoms of the dithiadiazolyl radical. This is consistent with a singly occupied molecular orbital (SOMO) of  $\pi^*$  character in which the local  $C_{2v}$  symmetry of the dithiadiazolyl ring produces a  $\pi^*$  orbital of  $a_2$  symmetry which is formally nodal at C.<sup>34</sup> The PND experiments also reveal some negative spin density in the  $p_z$  orbital of the carbon atom which is induced by spin polarization. In an unrestricted Hartree-Fock formalism, in which alpha (spin up) and beta (spin down) orbitals are allowed to have a different spatial distribution, the spin-polarization phenomenon arises from the electronic exchange interaction, which is non-null only between electrons with parallel spins, decreasing their energies. The exchange interaction between the alpha orbitals and the SOMO orbital partially counteracts their electrostatic repulsion allowing the alpha orbitals to have a higher overlap with the SOMO orbital than the beta orbitals. Therefore, the resulting different spatial distribution between alpha and beta orbitals produces a polarized negative spin density in some regions with a low overlap with the SOMO. The spin density populations determined by PND are in very good agreement with the values predicted by DFT studies and also from the EPR and ENDOR estimates of the unpaired spin density distributions around the N and F sites.

While the two modeling approaches produce broadly similar results, there are a few subtle differences. The most marked of these is the relative orientation of the N  $p_z$  orbital with respect to the heterocyclic plane. In the wave-function approach, the only significant orbital coefficient for the sulfur atom is the  $p_z$  one, consistent with the origin of the spin density. However, additional and significant  $p_x$  and  $p_y$  orbital coefficients at N are required to map the spin density satisfactorily. This leads to a “real”  $p_z$  orbital which is noncoin-

cident with respect to the *z* axis of the reference system, producing a nonzero projection on the other orbitals. This inclination can be clearly observed in the projection of the sulfur and nitrogen spin density distribution on the *yz* plane (see Fig. 2). Within this hypothesis, the tilt angle for the  $p_z$  orbital is 25°. The physical origin of this distortion could be attributed to the proximity of the fluorine atom in the *ortho* position of the perfluoraryl ring. Because of the twisting between the two rings, the fluorine atoms are not in the plane of the heterocyclic ring and electrostatic repulsions with one of the two lobes of the N  $2p_z$  orbital may lead to this asymmetric spin density distribution. Conversely, the wave-function approach may simply not be well adapted to describe the experimental spin density due to its strong geometric constraints. Within the Linear combination of atomic orbitals (LCAO-MO) approach, the nature of a  $\pi^*$  MO is substantially distorted from the parent MOs with build up of electron density away from the S and N atoms.

In contrast, the multipolar-expansion approach (see Figs. 4 and 5) removes the geometric constraints enforced by the wave-function approach and removes the inclination of the spin density on the N site. In addition, the multipolar-expansion approach models the anticipated displacement of the spin density on the S site away from neighboring sulfur and nitrogen atoms consistent with the antibonding nature of the SOMO orbital (Fig. 2). It is noteworthy that negative spin density is now observed between the sulfur atoms and also between the sulfur and nitrogen atoms. This negative spin density could be due to polarization effects produced by the SOMO orbital on the other doubly occupied molecular orbitals but may also be a spurious effect of the model trying to fit the displacement of the spin density away from the bonds to the sulfur atom.

Finally, an interesting characteristic of the obtained spin density is its more extended nature around the S atoms with respect to the N atoms, as can be observed in Figs. 4 and 5, considering that the spin populations on S and N are of the same order. In other polarized neutron-diffraction experiments on nitronyl nitroxide radicals,<sup>28</sup> the extension of the spin density was similar around the O and N atoms (also with spin populations of the same order). This result supports our initial hypothesis that sulfur-based free radicals can show more extended spin densities what, therefore, can favor the magnetic interactions.

### C. DFT spin density distribution

A number of theoretical studies have been undertaken on the dithiadiazolyl ring. Initial studies using simple Hückel and semiempirical methods modified neglect of differential overlap (MNDO) correctly identified the  $a_2$  symmetry of the SOMO and additional studies by Boeré found excellent correlations between the energy of the SOMO and the redox potential of the radical for a family of closely related phenyl-substituted dithiadiazolyls.<sup>35</sup> Detailed *ab initio* studies probed the  $\pi^*$ - $\pi^*$  dimerization energy and revealed that the energetics were strongly dependent on the basis set employed.<sup>36</sup> Recently DFT studies have been employed to model the spin density distribution in a number of perfluoro-

TABLE VII. Spin populations on the N and F sites in **2** determined by EPR/ENDOR studies, in comparison with PND and DFT calculations.

	EPR/ENDOR		Total (%)		
	% <i>s</i> character	% $\pi$ character	EPR	PND	DFT
N	0.81	23.41	24.22	24.5	22.4
<i>Ortho</i> -F	0.01	0.22	0.23	0	0
<i>Meta</i> -F		0.02	0.02	0	0

rophenyl derivatives.<sup>26</sup> These indicated that there was little spin density population on atoms other than those in the dithiadiazolyl ring. In the current study, our calculations have allowed us to verify these previous *ab initio* results.<sup>26</sup> In addition, the complementary nature of the PND, EPR, and ENDOR techniques to determine experimentally the spin density distribution allows an excellent comparison of theoretical and experimental studies. In particular, these calculations may also probe the negative spin densities on the C site and between heteroatoms in the dithiadiazolyl ring in order to determine whether these are artifacts of the multipolar-expansion model.

The excellent agreement between calculations based on the periodic system and on the isolated molecule models implies that the spin density distribution of the radical is not strongly affected by the environment. Indeed, these DFT Mulliken atom-centered spin populations are in excellent agreement with the PND results, confirming that the majority of the spin density distribution is localized on the dithiadiazolyl ring. These results are also in agreement with the previous DFT calculations.<sup>26</sup> However, the multipolar analysis of the PND also revealed important information on the spin density distribution between the atoms, particularly the buildup of negative spin density between the heteroatoms in the dithiadiazolyl ring. The spin density distribution from the *ab initio* calculation confirms the  $p_z$  nature of the spin density and the spin density displacement for the sulfur atoms (Fig. 5). It also correctly reflects the sign and magnitude of the negative spin density on the C  $p_z$  orbital induced through spin polarization. In addition, it also reflects the negative spin density distribution in the plane of the dithiadiazolyl ring observed in the multipolar analysis of the PND data. However, the value of this negative spin density is much smaller than that observed in the PND experiment.

The DFT calculations also indicate substantially less spin density on the substituent group, in agreement with previous calculations.<sup>26</sup> While the spin density on the phenyl C atoms is small, there is a notable alternation of signs in the spin populations for successive carbon atoms of the aryl ring, typical of the polarization effect along carbon chains.

#### D. EPR and ENDOR Studies

The hyperfine splitting observed in EPR spectroscopy arises through an isotropic Fermi contact interaction and a through-space dipole-dipole (anisotropic) interaction. In solution, the EPR spectra are rotationally averaged and reflect

only the isotropic contribution to the spin density distribution whereas frozen-solution measurements reflect both the isotropy and anisotropy in the spin density distribution. A number of theoretical studies have utilized this approach to resolve spin density distributions in terms of an isotropic *s*-character component and anisotropy arising from *p* (or *d* or *f*) orbital contributions. Here the percentage *s* character on a given nucleus E is simply related to the observed hyperfine interaction (in megahertz) and a theoretical parameter A which reflects the hyperfine coupling which would be expected for 100% spin density in that orbital,<sup>37</sup>

$$\rho_s = \frac{100a_{iso}}{A}. \quad (7)$$

The axial anisotropy can be related in a similar way to a theoretical parameter, *P* and an orbital reduction factor to accommodate whether the anisotropy arises out of *p*, *d*, or *f* character.<sup>37</sup> For rhombic systems, such as **2**, this axial anisotropy can be approximated to  $[a_1 - 1/2(a_2 + a_3)]$ . This yields

$$\rho_s = \frac{(1/3)[a_3 - (a_1 + a_2)/2]100}{2P/5}. \quad (8)$$

Using the theoretical values<sup>37</sup> and the observed hyperfine interactions to both N and F nuclei, the calculated spin populations on the N, F(1) and F(2) sites are given in Table VII.

The value of the spin population on the N site is in excellent agreement with those determined by PND and *ab initio* DFT studies. The values for the spin populations on the two chemically distinct F atoms are orders of magnitude lower, in agreement with the predominant localization of the spin density on the dithiadiazolyl ring.

#### V. CONCLUSIONS

The current studies have made use of a series of complementary experimental (polarized neutron diffraction coupled with EPR and ENDOR spectroscopies) and *ab initio* DFT techniques in order to probe the spin density distributions in the organic ferromagnet *p*-O<sub>2</sub>NC<sub>6</sub>F<sub>4</sub>CNSSN. The polarized neutron-diffraction studies reveal that the spin density is almost entirely located on the sulfur and nitrogen atoms of the dithiadiazolyl ring in a  $p_z$ -orbital-type distribution with the *z* axis perpendicular to the ring, and a small negative spin density on the C atom arising out of spin polarization. These studies also show that the spin density is displaced away from both atoms and bonds within the dithiadiazolyl ring in

accord with the antibonding nature of the SOMO determined by *ab initio* DFT calculations. Both the experimental and theoretical studies also indicate small negative spin densities in the plane of the heterocyclic ring.

The spin density on the N site is independently estimated by EPR studies and is quantitatively in very good agreement with the spin densities determined by PND and DFT. In addition, ENDOR studies reveal the small spin density distributions on the perfluorophenyl ring via hyperfine interactions to the two chemically inequivalent F atoms. The modeled experimental spin densities are in good agreement with those determined by DFT. The large displacement of the spin density distribution away from the dithiadiazolyl ring (associated with the  $\pi^*$  nature of the SOMO and enhanced by the diffuse nature of the sulfur  $3p$  orbitals) coupled with the electrostatically favorable S $\cdots$ N contacts between radicals should favor a direct exchange mechanism between radical centres. For instance, in the case of the studied nitro derivative, four different direct exchange magnetic interactions are possible through intermolecular contacts among atoms of neighbor dithiadiazolyl rings whereas other intermolecular contacts will be inefficient to propagate relevant magnetic

interactions due to the low spin populations in the atoms out of the dithiadiazolyl ring.

This exhaustive and complete study of the spin density in the prototype system *p*-O<sub>2</sub>NC<sub>6</sub>F<sub>4</sub>CNSSN will help to better understand the magnetic interaction mechanism, and therefore the magnetic behavior, in all the members of the series *p*-X-C<sub>6</sub>F<sub>4</sub>CNSSN. This is due to the fact that the substituents change the relative spatial orientation of the molecules (particularly the CNSSN rings) without any significant modification of the spin density distribution. Moreover, the radially expanded nature of the spin density at sulfur supports the hypothesis that inclusion of heavier *p*-block elements will favor higher magnetic ordering temperatures.

#### ACKNOWLEDGMENTS

This work has been funded by the Spanish MICINN and FEDER, Projects No. MAT2009-13977-C03-01, No. MAT2007-61621 and by Consolider Programme in Molecular Nanoscience Ref. CSD2007-00010 and by the U.K. EPSRC agency. In addition, the authors thank the Institut Laue Langevin for neutron beam time allocation on D9 and D3 instruments.

\*javier.campo@unizar.es

- <sup>1</sup>M. Kinoshita, P. Turek, M. Tamura, K. Nozawa, D. Shiomi, Y. Nakazawa, M. Ishikawa, M. Takahashi, K. Awaga, T. Inabe, and Y. Maruyama, *Chem. Lett.* **20**, 1225 (1991).
- <sup>2</sup>J. M. Rawson, A. J. Banister, and I. Lavender, *Adv. Heterocycl. Chem.* **62**, 137 (1995).
- <sup>3</sup>W. Fujita, K. Awaga, Y. Nakazawa, K. Saito, and M. Sorai, *Chem. Phys. Lett.* **352**, 348 (2002).
- <sup>4</sup>W. Fujita and K. Awaga, *Chem. Phys. Lett.* **388**, 186 (2004).
- <sup>5</sup>C. M. Robertson, A. A. Leitch, K. Cvrkalj, R. W. Reed, D. J. T. Myles, P. A. Dube, and R. T. Oakley, *J. Am. Chem. Soc.* **130**, 14791 (2008).
- <sup>6</sup>A. J. Banister, N. Bricklebank, I. Lavender, J. M. Rawson, C. I. Gregory, B. K. Tanner, W. Clegg, M. R. J. Elsegood, and F. Palacio, *Angew. Chem., Int. Ed. Engl.* **35**, 2533 (1996); F. Palacio, G. Antorrena, M. Castro, R. Burriel, J. M. Rawson, J. N. B. Smith, N. Bricklebank, J. Novoa, and C. Ritter, *Phys. Rev. Lett.* **79**, 2336 (1997).
- <sup>7</sup>M. Mito, T. Kawae, K. Takeda, S. Takagi, Y. Matsushita, H. Deguchi, J. M. Rawson, and F. Palacio, *Polyhedron* **20**, 1509 (2001).
- <sup>8</sup>G. Antorrena, F. Palacio, J. E. Davies, M. Hartley, J. M. Rawson, J. N. B. Smith, and A. Steiner, *Chem. Commun. (Cambridge)* **1999**, 1393.
- <sup>9</sup>J. M. Rawson, J. Luzon, and F. Palacio, *Coord. Chem. Rev.* **249**, 2631 (2005).
- <sup>10</sup>A. Alberola, R. J. Less, F. Palacio, C. M. Pask, and J. M. Rawson, *Molecules* **9**, 771 (2004).
- <sup>11</sup>A. Alberola, R. J. Less, C. M. Pask, J. M. Rawson, F. Palacio, P. Oliete, C. Paulsen, A. Yamaguchi, R. D. Farley, and D. M. Murphy, *Angew. Chem., Int. Ed. Engl.* **42**, 4782 (2003).
- <sup>12</sup>J. Luzon, J. Campo, F. Palacio, G. J. McIntyre, A. E. Goeta, E. Ressouche, C. M. Pask, and J. M. Rawson, *Physica B* **335**, 1 (2003); J. Luzon, J. Campo, F. Palacio, G. J. McIntyre, A. E. Goeta, C. M. Pask, and J. M. Rawson, *Polyhedron* **22**, 2301 (2003).
- <sup>13</sup>R. T. Boeré, R. T. Oakley, and R. W. Reed, *J. Organomet. Chem.* **331**, 161 (1987).
- <sup>14</sup>M. S. Cooper, H. Heaney, A. J. Newbold, and W. R. Sanderson, *Synlett* 533 (1999).
- <sup>15</sup>J. C. Matthewman, P. Thompson, and P. J. Brown, *J. Appl. Crystallogr.* **15**, 167 (1982).
- <sup>16</sup>L. Koester, *Springer Tracts Mod. Phys.* **80**, 1 (1977).
- <sup>17</sup>J. Cosier and A. M. Glazer, *J. Appl. Crystallogr.* **19**, 105 (1986).
- <sup>18</sup>SMART, Data Reduction Software, version 5.0. Bruker Analytical X-ray Instruments Inc., Madison, WI (1998).
- <sup>19</sup>SAINT, Data Reduction Software, version 5.0. Bruker Analytical X-ray Instruments Inc., Madison, WI (1998).
- <sup>20</sup>SHELXTL, version 5.1. Bruker Analytical X-ray Instruments Inc., Madison, WI (1998).
- <sup>21</sup>H. D. Flack, *Acta Crystallogr., Sect. A: Found. Crystallogr.* **39**, 876 (1983).
- <sup>22</sup>G. C. Hurst, T. A. Henderson, and R. W. Kreilick, *J. Am. Chem. Soc.* **107**, 7294 (1985); T. A. Henderson, G. C. Hurst, and R. W. Kreilick, *ibid.* **107**, 7299 (1985).
- <sup>23</sup>E. Ressouche, J. X. Boucherle, B. Gillon, P. Rey, and J. Schweizer, *J. Am. Chem. Soc.* **115**, 3610 (1993).
- <sup>24</sup>P. J. Brown, A. Capiomont, B. Gillon, and J. Schweizer, *J. Magn. Magn. Mater.* **14**, 289 (1979).
- <sup>25</sup>N. K. Hansen and P. Coppens, *Acta Crystallogr., Sect. A: Cryst. Phys., Diffr., Theor. Gen. Crystallogr.* **34**, 909 (1978).
- <sup>26</sup>P. J. Alonso, G. Antorrena, J. I. Martinez, J. J. Novoa, F. Palacio, J. M. Rawson, and J. N. B. Smith, *Appl. Magn. Reson.* **20**, 231 (2001).

- <sup>27</sup>N. J. Fitzpatrick and G. H. Murphy, *Inorg. Chim. Acta* **87**, 41 (1984).
- <sup>28</sup>A. Zheludev, V. Barone, M. Bonnet, B. Delley, A. Grand, E. Ressouche, P. Rey, R. Subra, and J. Schweizer, *J. Am. Chem. Soc.* **116**, 2019 (1994).
- <sup>29</sup>A. Zheludev, A. Grand, E. Ressouche, J. Schweizer, B. G. Morin, A. J. Epstein, D. A. Dixon, and J. S. Miller, *J. Am. Chem. Soc.* **116**, 7243 (1994).
- <sup>30</sup>B. Delley, *J. Chem. Phys.* **92**, 508 (1990).
- <sup>31</sup>J. P. Perdew, J. A. Chevary, S. H. Vosko, K. A. Jackson, M. R. Pederson, D. J. Singh, and C. Fiolhais, *Phys. Rev. B* **46**, 6671 (1992).
- <sup>32</sup>S. A. Fairhurst, K. M. Johnson, L. H. Sutcliffe, K. F. Preston, A. J. Banister, Z. V. Hauptman, and J. Passmore, *J. Chem. Soc. Dalton Trans.* **1986**, 1465 ; G. K. MacLean, J. Passmore, M. N. S. Rao, M. J. Schriver, P. S. White, D. Bethel, S. Pilkington, and L. H. Sutcliffe, *ibid.* **1985**, 1405 ; E. G. Awere, N. Burford, C. Mailer, J. Passmore, M. J. Schriver, P. S. White, A. J. Banister, H. Oberhammer, and L. H. Sutcliffe, *J. Chem. Soc., Chem. Commun.* **1987**, 66.
- <sup>33</sup>J. G. Stark and H. G. Wallace, *Chemistry Data Book* (J. Murray, London, 1980).
- <sup>34</sup>J. Campbell, D. Klapstein, P. F. Bernath, W. M. Davis, R. T. Oakley, and J. D. Goddard, *Inorg. Chem.* **35**, 4264 (1996).
- <sup>35</sup>R. T. Boéré, K. H. Moock, and M. Parvez, *Z. Anorg. Allg. Chem.* **620**, 1589 (1994).
- <sup>36</sup>A. W. Cordes, R. C. Haddon, W. M. Davis, R. H. de Laat, S. H. Glarum, J. D. Goddard, R. C. Haddon, R. G. Hicks, D. K. Kennepohl, R. T. Oakley, S. R. Scott, and N. P. C. Westwood, *J. Am. Chem. Soc.* **115**, 7232 (1993).
- <sup>37</sup>J. R. Morton and K. F. Preston, *J. Magn. Reson.* **30**, 577 (1978).